



# Unsteady influences of blade loading distribution on secondary flow of ultra-high-lift LPT

Xiao Qu <sup>a,b</sup>, Yingjie Zhang <sup>a,b</sup>, Xingen Lu <sup>a,b</sup>, Junqiang Zhu <sup>a,b</sup>, Yanfeng Zhang <sup>a,b,\*</sup>

<sup>a</sup> Key Laboratory of Light-Duty Gas-Turbine, Institute of Engineering Thermophysics, Chinese Academy of Sciences, Beijing, 100190, China

<sup>b</sup> University of Chinese Academy of Sciences, Beijing, 100190, China



## ARTICLE INFO

### Article history:

Received 29 July 2019

Received in revised form 30 September 2019

Accepted 9 November 2019

Available online 14 November 2019

### Keywords:

Secondary flow

Blade loading distribution

Ultra-high-lift

Low-pressure turbine

## ABSTRACT

Experimental measurements were performed to study the influence of blade loading distribution on the aerodynamic performance of an ultra-high-lift low-pressure turbine cascade ( $Zw = 1.58$ ) in the presence and absence of incoming wakes. The flow structures in front-loaded and aft-loaded blade passages were comprehensively compared at various Reynolds numbers. Furthermore, the flow mechanisms responsible for the effect of the blade loading distribution on the secondary flow were discussed in detail through numerical calculations. At the low Reynolds number of 25,000, weaker secondary flow was observed for the aft-loaded blade under steady conditions owing to the lower cross-passage pressure gradient compared to the front-loaded blade. Unsteady wakes clearly improved the throughflow characteristics of the cascade passage, increased the blade loading, and strengthened the secondary flow in the aft-loaded blade passage. At the high Reynolds number of 100,000, unsteady wakes delayed generation of the passage vortex in both the front-loaded and aft-loaded blade passages and clearly weakened the secondary flow. The experimental results revealed that the upstream wakes reduced the strength of the passage vortex core in the aft-loaded and front-loaded blade profiles by 21.6% and 17.5%, respectively.

© 2019 Elsevier Masson SAS. All rights reserved.

## 1. Introduction

Modern civil aircraft engines typically possess a high bypass ratio for increased efficiency [1]. High-bypass-ratio engines require high output power from the low-pressure turbine (LPT) to drive the fan [2], which necessitates a greater number of blade rows and lower rotational speed of the LPT. However, multistage LPTs possess a higher weight. The LPT typically accounts for approximately one-third of the total weight of the entire engine [3]. Increasing the blade loading is an effective method for reducing the weight of LPTs [4]. Decreasing the LPT weight by 8% can reduce the specific fuel consumption by 1% [5]. High-lift LPT have an increased adverse pressure gradient. In addition, the Reynolds number of an LPT decreases under high-altitude cruising conditions and can be as low as  $3 \times 10^4$ – $5 \times 10^4$ , which is considerably less than the critical Reynolds number [6]. A laminar boundary layer is formed under such low Reynolds numbers, which is unable to overcome the greater adverse pressure gradient in high-lift LPTs. Therefore, increasing the LPT blade loading may lead to flow separation, and increase profile losses and endwall losses.

Several effective flow control methods are already applied to reduce profile losses and secondary losses. To suppress profile losses, researchers have proposed numerous measures to mitigate or prevent suction side separation, such as surface roughness [7], jets [8], plasma actuators [9], and dimples [10,11]. To reduce endwall losses, several passive control methods have been investigated, such as fences [12], leading edge bulbs [13], fillets [14,15], non-axisymmetric endwall contouring [16], and recently bio-inspired micro-texture on rotor blade [17]. However, various problems must be overcome before these techniques can be applied to actual aircraft engines, such as improving the durability, cost, off-design performance, and so on. Another strategy for controlling the separation is to optimize blade loading distribution such that the peak position of blade aerodynamic loading is located near either the leading edge (front-loaded) or trailing edge (aft-loaded). Aft-loaded blades have been reported to reduce endwall losses [18, 19], but can lead to open separation on the suction side owing to the strong adverse pressure gradient at low Reynolds numbers. The adverse pressure gradient was reduced for front-loaded blades on the aft portion of the blade suction surface. McQuilling [20] reported that front-loaded blades can be designed at very high loading levels and the separation bubble can remain closed even at low Reynolds numbers. However, high-lift front-loaded blades may lead to greater secondary losses.

\* Corresponding author.

E-mail address: [zhangyf@iet.cn](mailto:zhangyf@iet.cn) (Y. Zhang).

## Nomenclature

FSTI	free-stream turbulence intensity	X	axial coordinate.....	mm
LPT	low-pressure turbine	y	pitchwise coordinate .....	mm
TKE	turbulence kinetic energy	$C_p$	static pressure loss coefficient	
PV	passage vortex	Y	total pressure loss coefficient	
PS	pressure surface	$Y_{mix}$	mixing loss of the cylindrical bars	
SS	suction surface	$Y_{tot}$	total losses	
SST	shear-stress transport	$Y_p$	profile losses	
Vph	pressure side leg of the horseshoe vortex	$\theta$	deviation angle .....	°
Re	Reynolds number	$\Delta t$	time step.....	s
$C_x$	axial chord..... mm	t	instantaneous time .....	s
$C\omega_s$	dimensionless streamwise vorticity	$\tau$	one period time.....	s
U	velocity..... m/s			

In multistage aircraft engine environments, unsteady wakes were considered one of the most important unsteady factors. Schulte and Hodson [21] demonstrated that the wake-boundary layer interaction can induce boundary layer transition and suppress separation. The wake-boundary layer interaction has received continuous attention from numerous scholars [22–24]. In recent years, the interactions between incoming wakes and secondary flow have also attracted interest. Schneider et al. [25] experimentally and numerically researched a two-stage low pressure turbine and showed that the flow field in rotor passage was significantly affected by the wakes and secondary vortex of upstream stator blade. Ciorciari et al. [26] also found that upstream wakes induced vortices to result in passage vortex and corner vortex periodic reduction. Furthermore, Qu et al. [27] and Lei et al. [28] studied wakes-secondary flow interaction, and found that incoming wakes can decrease the horseshoe vortex.

In the present study, detailed experimental measurements in ultra-high-lift LPT cascades were conducted to investigate the effect of the blade loading distribution on the separation bubble and secondary flow in the presence and absence of wakes. Flow field data on measuring plane were recorded through a seven-hole probe. Flow structures in front-loaded and aft-loaded blade passages were comprehensively compared at various Reynolds numbers. Furthermore, the flow mechanisms responsible for blade loading distribution affecting on the secondary flow were examined via numerical calculations at Reynolds number of 100,000.

## 2. Experimental and numerical approaches

### 2.1. Test rig introduction

The experimental investigation was conducted in a multifunctional low-speed wind tunnel. This low-speed wind tunnel is of typical construction with a centrifugal fan, divergent section, settling section, contraction section, and unsteady test section. The overall configuration of unsteady test section is depicted in Fig. 1. Inlet flow uniformity was controlled by adjusting bottom flap and upstream top flap, and periodicity of outlet flow can be assured through adjusting downstream tailboards. A hot-wire anemometer was applied to measure the free-stream turbulence intensity (FSTI) upstream of the cascade (1.3 of axial chord). The background FSTI of the low-speed wind tunnel was approximately 0.4%. For the experimental measurements, the turbulence grid was installed upstream of the wind tunnel to increase FSTI to approximately 2.2%. Moving bars upstream of the cascade can produce unsteady wakes. A seven-hole probe was installed at cascade exit (approximately 40% of axial chord), as indicated in Fig. 2. The geometric and aerodynamic parameters of aft-loaded IET-A and front-loaded IET-F are listed in Table 1. All parameters are the same except blade loading distribution.

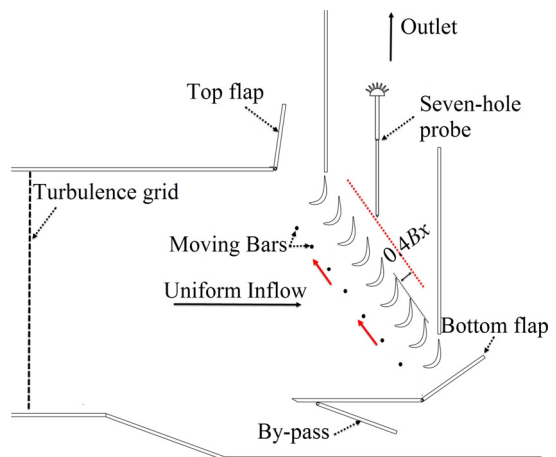


Fig. 1. Overall configuration of unsteady test section.

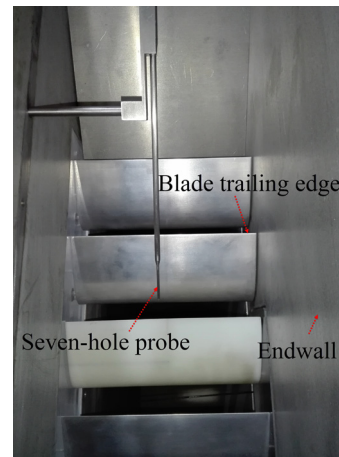


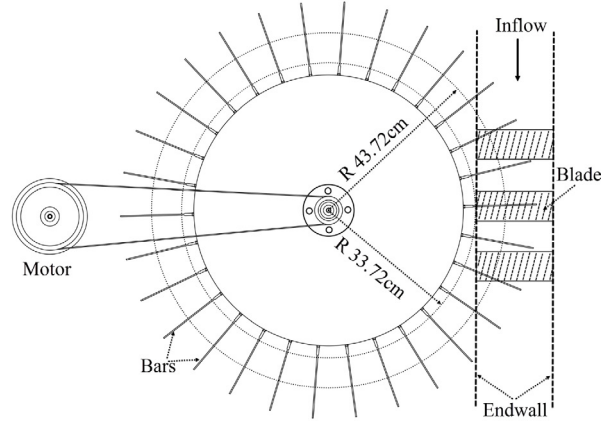
Fig. 2. Photograph of the seven-hole probe.

Table 1  
Main parameters of the tested cascades.

Parameter	Aft-loaded IET-A/ Front-loaded IET-F
Axial chord, $C_x$ [mm]	75.4
Pitch, $s$ [mm]	91.58
Span, H [mm]	200
Blade aspect-ratio	2.2
Zweifel number	1.58
Bar diameter [mm]	1.8
Bar-cascade axial gap [mm]	0.6 $C_x$



(a) Photograph of the wake generator rig



(b) Plan view of the wake generator rig

Fig. 3. Wake generator rig.

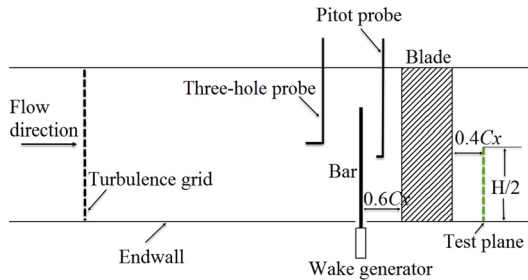


Fig. 4. Position of the three-hole pressure probe and pitot probe.

## 2.2. Wake generator equipment

Cylindrical bars and LPT blades have almost the similar wake flow. The wake generator used in the present study consisted of a solid disk with cylindrical bars, as shown in Fig. 3. The wheel was driven using an AC motor. A frequency controller was used to adjust the speed of the AC motor to control the passing frequency of the wakes. The root diameter of the wheel was 67.44 cm, and the length and diameter of the cylindrical bars were 200 cm and 1.8 cm, respectively. To precisely evaluate the effect of the incoming wakes on the flow field inside cascade passage, the mixing loss of the cylindrical bars was subtracted from the total losses in all cases. Therefore, the mixing loss of the cylindrical bars ( $Y_{mix}$ ) was measured through a pitot probe and a three-hole probe, as depicted in Fig. 4. Additionally, to prevent leakage through the gap for the bars in the endwall, the wheel was surrounded with a box to ensure pressure balance inside the wind tunnel and box.

The mixing loss of the cylindrical bars was defined as follows:

$$Y_{mix} = \frac{P_{o,i} - P_{o,pitot}}{P_{o,i} - P_{s,i}} \quad (1)$$

where  $P_{o,i}$  and  $P_{s,i}$  were the inlet total pressure and static pressure at midspan, which were obtained through three-hole probe.  $P_{o,pitot}$  was local total pressure, which was measured by pitot probe.

## 2.3. Instrumentation

A seven-hole pressure probe with a head diameter of approximately 3 mm was used to obtain the total pressure, static pressure, and the three components of velocity in the axial, pitchwise, and spanwise directions. Total pressure, static pressure, and velocity of cascade inlet were obtained by Pitot probe. Three-hole pressure probe was used to monitor inlet flow uniformity and measure

inlet velocity distribution. The calibration of the seven-hole and three-hole pressure probes was conducted in a calibration wind tunnel. The data from the pressure probes were collected using a Model 9116 Intelligent Pressure Scanner (PSI), with a maximum pressure range and acquisition frequency of 2.5 kPa and 500 Hz, respectively. A digital barometer (XE66YM3) and digital thermometer (HG429-SWJ-IC) were also used in the experimental measurements, and the speed of the wheel was measured using a speed sensor.

The test system consisted of an industrial personal computer (IPC), motion system, and test equipment. The control signal was transmitted from the IPC to the controller, subjected to analog-to-digital conversion, and then transmitted to the stepping motor driving the two-dimensional traverse mechanism. Pressure probes were installed at the traverse mechanism, including the pitot probe, three-hole and seven-hole pressure probes. The IPC was used to collect the data from the Intelligent Pressure Scanner, barometer, and thermometer.

The error range for seven-hole probe was  $\pm 1\%$ , and the accuracy of the stepping motor was  $\pm 0.1$  Hz. The data from pressure probes is collected by Pressure Systems Incorporated, and the error was less than  $\pm 0.5\%$  in the present measurements. Additionally, variance of pressure fluctuation is also the error at the same measuring point.

## 2.4. Numerical method

The CFX 13.0 was used to calculate three dimensional viscous flow in the turbine cascade [29]. To increase the calculation speed, the computational domain was set as half of the cascade span in all computations. The "H-O-H" and "O" mesh topologies were used for the cascade domain and bar domain, respectively, as depicted in Fig. 5.

The analysis of numerical errors was conducted in Fig. 6. Ultimately, a two-equation turbulence model SST  $k-\omega$  was used to solve incompressible Navier-Stokes equations. Some previous studies [30,31] also found SST turbulence model was suitable for computing secondary flow. The "gamma-theta" transition model was also adopted for calculating more accurately the laminar-to-turbulent transitional flow, which exhibited good agreement with the experimental result, as shown in Fig. 6(a).

Verification of grid dependency was indicated in Fig. 6(b).  $C_{SKE}$  is the non-dimensional secondary kinetic energy, which is defined in [24]. Approximately 2.5 million points were adopted for the stationary cascade domain. The grid points distributions for moving bar and stationary cascade in the spanwise, pitchwise and streamwise directions were  $33 \times 45 \times 97$ ,  $105 \times 57 \times 349$ , respectively.

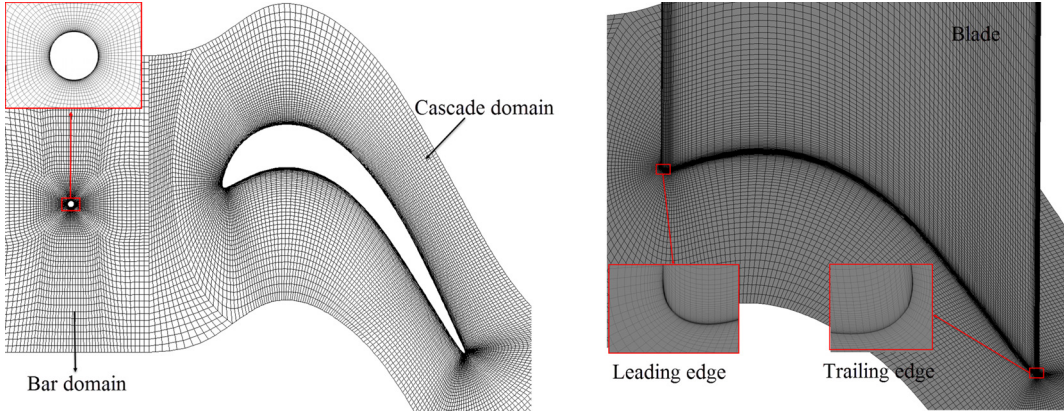


**Fig. 5.** Structured mesh topology for the cascade passage (IET-F).

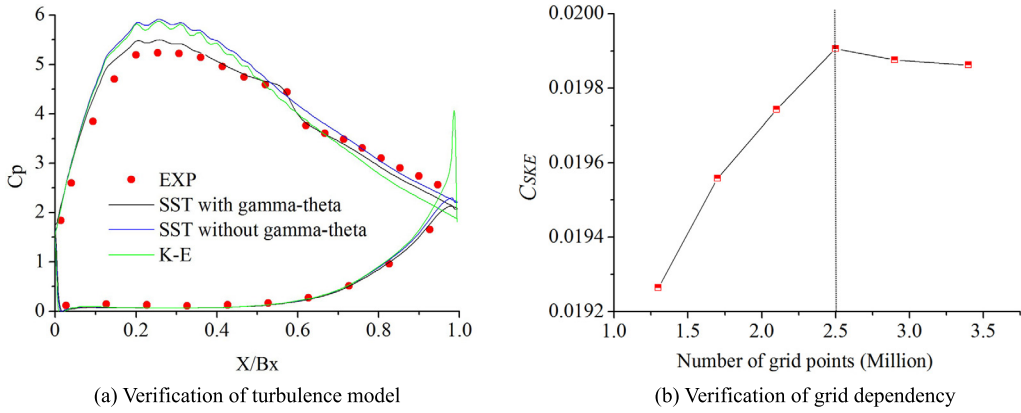


**Fig. 6.** Analysis of numerical errors (IET-F). (For interpretation of the colors in the figures, the reader is referred to the web version of this article.)

At cascade inlet, freestream turbulence, flow angle and spanwise velocity distribution from the endwall to midspan were imposed, inlet boundary distribution was given according to experimental result, and the standard atmospheric pressure was specified as the outflow boundary condition. In order to calculate accurately the flow characteristics of upstream wakes at  $Re = 100,000$ , the calculated frequency should be more 20 times than the frequency of Carmen Vortex Street downstream bars, the time step ( $\Delta t$ ) is  $2.5 \times 10^{-5}$ , the wake passing frequency is approximately 1.2. According to the requirements of the SST k- $\omega$  model, the maximum non-dimensional wall distance ( $y^+$ ) was less than 1 at the first node from the solid walls.

The development of blade suction surface separation and secondary flow structures are both strongly affected by the blade loading. Fig. 7 indicates blade pressure coefficient ( $C_p$ ) and pitchwise mass-averaged deviation angle ( $\theta$ ) comparison between experimental and computational results under Reynolds number of 100,000. Experimental data were shown with error bars. The predicted blade loading distributions and experimental results were in good agreement, and the size and position of the separation bubble and secondary vortices were predicted accurately. Overall, these results demonstrate the reliability of the numerical methods applied in this study.

## 2.5. Data processing

The static pressure coefficient is defined as follows:

$$C_p = \frac{P_{o,i} - P_s}{P_{o,i} - P_{s,i}} \quad (2)$$

The total pressure loss coefficient is defined as follows:

$$Y = \frac{P_{o,i} - P_{o,loc}}{P_{o,i} - P_{s,i}} \quad (3)$$

where  $P_{o,loc}$  and  $P_s$  are local total pressure and static pressure, respectively.

Additionally, in a Cartesian coordinate system, the fluid in cascade was assumed to be steady, inviscid and ignoring volume force, the computing method of vorticity described by Gregory-Smith et al. [32] was used in this study to derive the vorticity components in the axial ( $\omega_x$ ), pitchwise ( $\omega_y$ ), and spanwise directions ( $\omega_z$ ). The vorticity vector  $\omega$  is defined as the curl of the velocity vector  $U$ , and  $u$ ,  $v$ , and  $w$  are the velocity components in the axial, pitchwise, and spanwise directions, respectively:

$$\omega = \nabla \times U \quad (4)$$

$$\omega_x = \frac{\partial w}{\partial y} - \frac{\partial v}{\partial z} \quad (5)$$

$$\omega_y = \frac{1}{u} (v \omega_x - \frac{1}{\rho} \frac{\partial P_0}{\partial z}) \quad (6)$$

$$\omega_z = \frac{1}{u} (\frac{1}{\rho z} \frac{\partial P_0}{\partial y} + w \omega_x) \quad (7)$$

The streamwise vorticity ( $\omega_s$ ) is defined as follows:

$$\omega_s = \frac{u \omega_x + v \omega_y + w \omega_z}{|U|} \quad (8)$$

The dimensionless streamwise vorticity ( $C\omega_s$ ) is defined as follows:

$$C\omega_s = \frac{\omega_s B_x}{|U|} \quad (9)$$

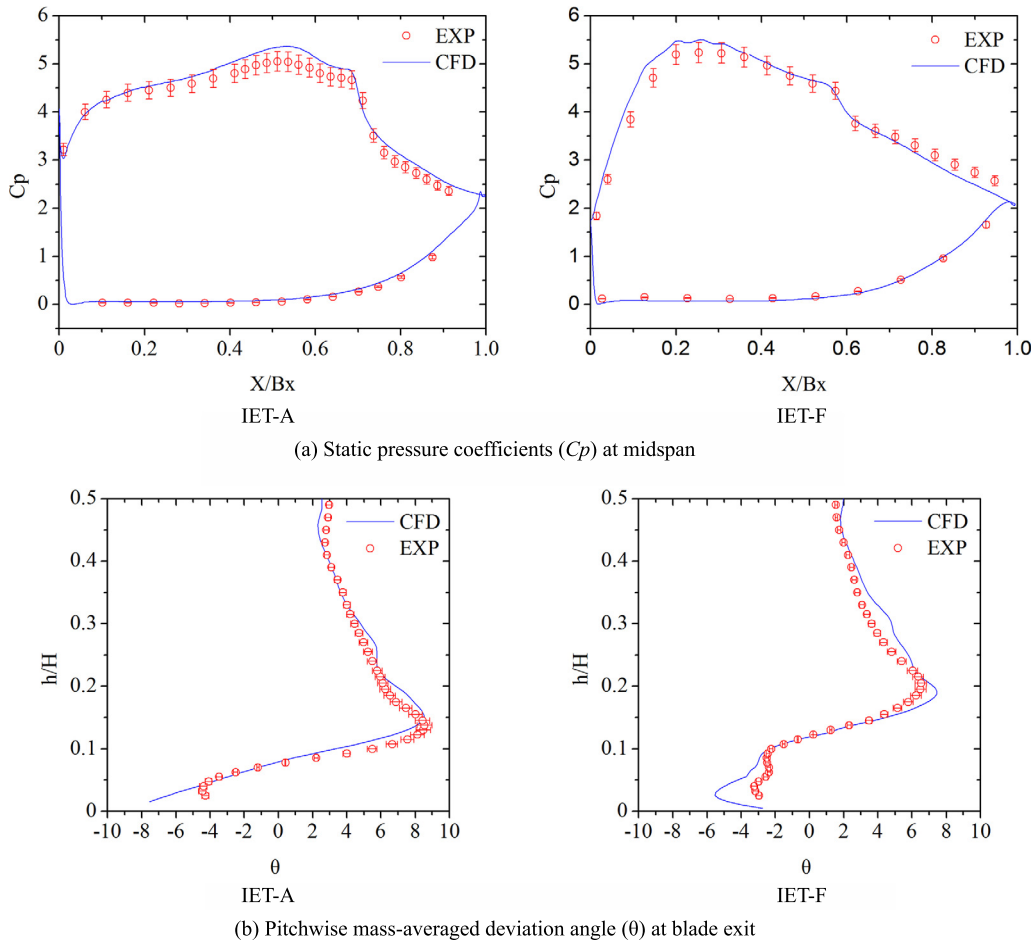


**Fig. 7.** Comparison of experimental and numerical static pressure coefficients at the blade surface and pitchwise mass-averaged deviation angle ( $\theta$ ) at blade exit; experimental data were shown with error bars.

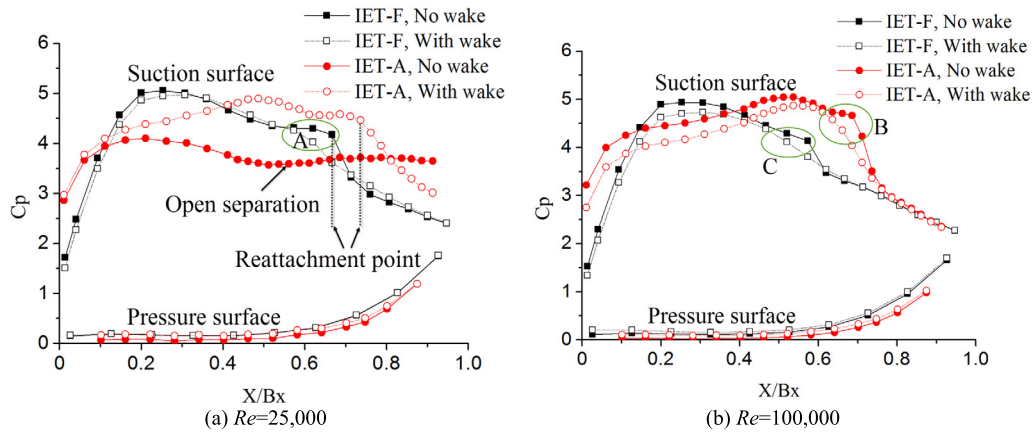


**Fig. 8.** Static pressure coefficients of the front-loaded and aft-loaded blades surfaces.

### 3. Results and discussion

#### 3.1. Influence of blade loading distribution on profile loss at midspan (EXP)

The static pressure coefficients at the surfaces of the ultra-high-lift front-loaded and aft-loaded blades at the midspan are plotted in Fig. 8. For the ultra-high-lift aft-loaded blade (IET-A), large-scale open separation occurred on the suction surface at low  $Re = 25,000$ , and wake passing caused reattachment of the separation bubbles, suppressed the separation bubbles, and increased

the blade loading at the suction side, because reattachment of open separations bubble increased flow area of cascade passage, increasing flow velocity of suction surface and decreasing pressure of suction side. At the high  $Re = 100,000$ , the suction side separation bubbles reattached and the maximum velocity occurred at approximately 54% of axial chord; after this position, static pressure coefficient gradually decreased and a pressure plateau appeared. Pressure plateau indicated existence of a laminar separation bubble. Incoming wakes essentially eliminated this pressure plateau, as indicated by the letter "B" in Fig. 8(b), by promoting the transition and reattachment of the separation bubbles. Ref. [33] has discussed

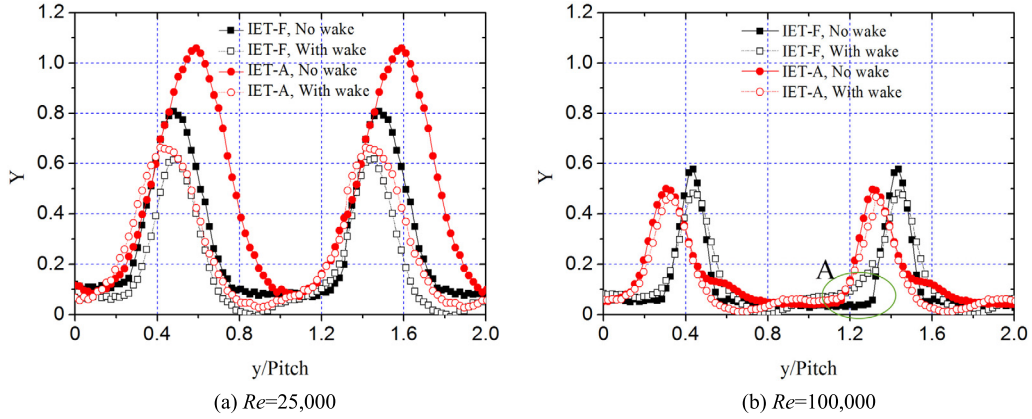


**Fig. 9.** Comparison of total pressure loss coefficients at the cascade exit.

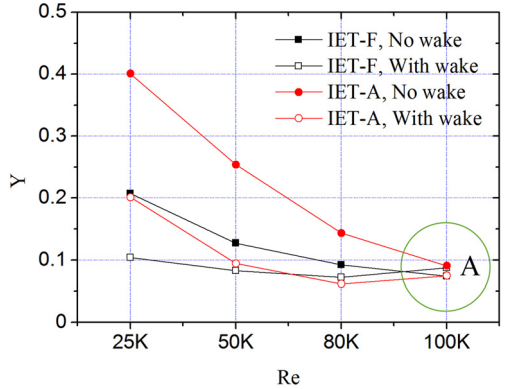


**Fig. 10.** Mass-averaged profile loss ( $Y_p$ ) distributions at the cascade exit (midspan).

in detail the interaction mechanisms between unsteady wakes and separation bubble. For the ultra-high-lift front-loaded blade (IET-F), the peak velocity occurred at approximately 25% of axial chord, and the reattachment position of the suction side separation bubble moved forward at  $Re = 100,000$ , indicating a smaller separation bubble, compared to the results obtained at  $Re = 25,000$  under steady conditions. Incoming wakes further suppressed the separation, as indicated by the letters "A" and "C" in Fig. 8. In addition, the unsteady wakes also introduced some low-momentum fluid, thereby decreasing the blade loading at the suction surface.

Fig. 9 shows a comparison of the total pressure loss coefficients ( $Y$ ) downstream of the cascade (40% of the axial chord) at blade midspan. The formation of a high-loss region at cascade exit is mainly related to the size of suction surface separation bubble. At low  $Re = 25,000$ , the width and height of the high-loss region downstream of the cascade were clearly greater than those at the high  $Re = 100,000$  owing to the larger suction surface separation bubble. This was particularly true for the aft-loaded blade, where the width of the high-loss region at the low Reynolds number of 25,000 accounted for approximately 80% of the entire passage owing to the open separation of blade suction side, which severely affects the aerodynamic performance of ultra-high-lift LPTs. Incoming wakes significantly suppressed both the width and height of the high-loss region downstream of the cascade at the low  $Re = 25,000$  for both the front-loaded and aft-loaded blades, whereas the influence of incoming wakes on the separation bubbles was not obvious at the high  $Re = 100,000$ . Furthermore, the presence of wakes increased the mixing loss of the free-flow region for the front-loaded blade, because of characteristics of wake's high turbulence and velocity defect, as indicated by the letter "A" in Fig. 9(b).

Fig. 10 shows the profile loss ( $Y_p$ ) distributions at various Reynolds numbers. The profile loss decreased gradually with in-

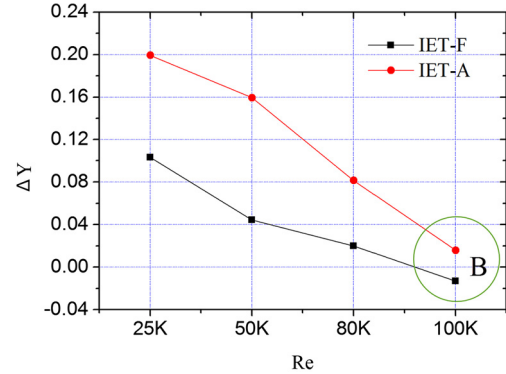


**Fig. 11.**  $\Delta Y_p$  distributions at the cascade exit (midspan).

crease of Reynolds number, this trend was also similar to Montomoli et al. [34] experimental results. Under steady conditions in the absence of wakes, the profile loss was greater for the aft-loaded blade than for the front-loaded blade. In particular, at the low  $Re = 25,000$ , the profile loss was approximately 50% greater for the aft-loaded blade than for the front-loaded blade. At the high  $Re = 100,000$ , the profile losses were similar owing to the generally small size of the suction surface separation bubble, as marked by the letter "A" in Fig. 10. Fig. 11 shows the distribution of  $\Delta Y_p$  at the cascade exit ( $\Delta Y_p = Y_{p,no-wake} - Y_{p,with-wake}$ ). The passing wakes exerted a greater influence on the aft-loaded blade than on the front-loaded blade, particularly at low Reynolds numbers; incoming wakes decreased the profile loss by approximately 50% at  $Re = 25,000$ . However, at the high  $Re = 100,000$ , the value of  $\Delta Y_p$  for the front-loaded blade in the presence of wakes was less than zero, as indicated by the letter "B" in Fig. 11, which indicates that the upstream wakes exerted a negative effect on the profile losses for the front-loaded blade, because the separation bubble on front-loaded blade suction surface is smaller than aft-loaded blade, although upstream wakes suppress the size of separation bubbles (Fig. 8(b)), the mixing loss of wakes is greater than separation loss decreased by wake for the front-loaded blade (Fig. 9(b)).

### 3.2. Influence of blade loading distribution on secondary flow (EXP)

For ultra-high-lift LPTs with different loading distributions, upstream wakes not only influence the suction surface boundary layer but also play an important part in endwall flow. Contour maps of the total pressure loss coefficient and streamwise vorticity coefficient at 40% of axial chord downstream of the cascade are presented in Fig. 12. At the low  $Re = 25,000$ , although the

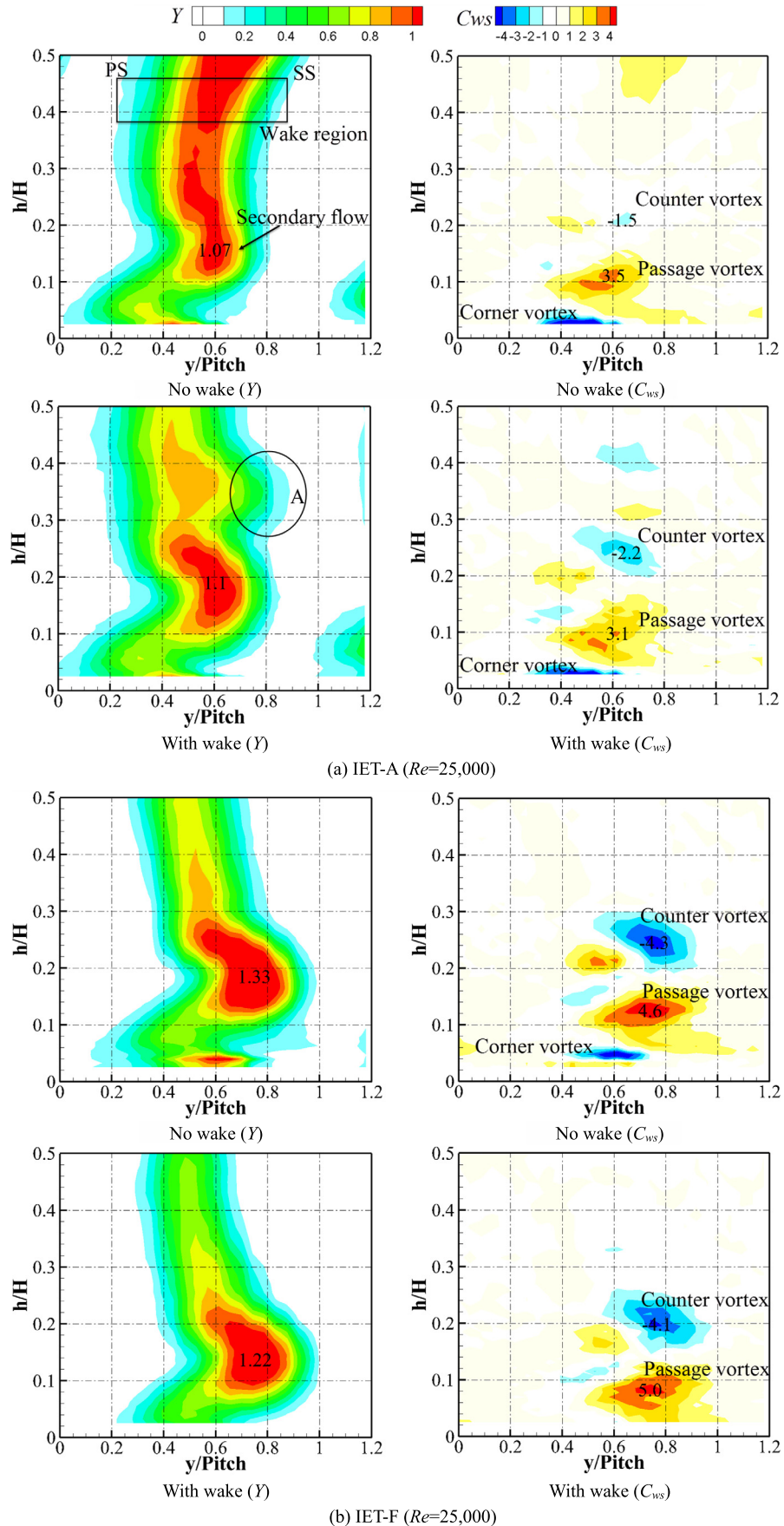


**Fig. 12.** Contour maps of the total pressure loss coefficient and streamwise vorticity coefficient 40% downstream cascade exit.

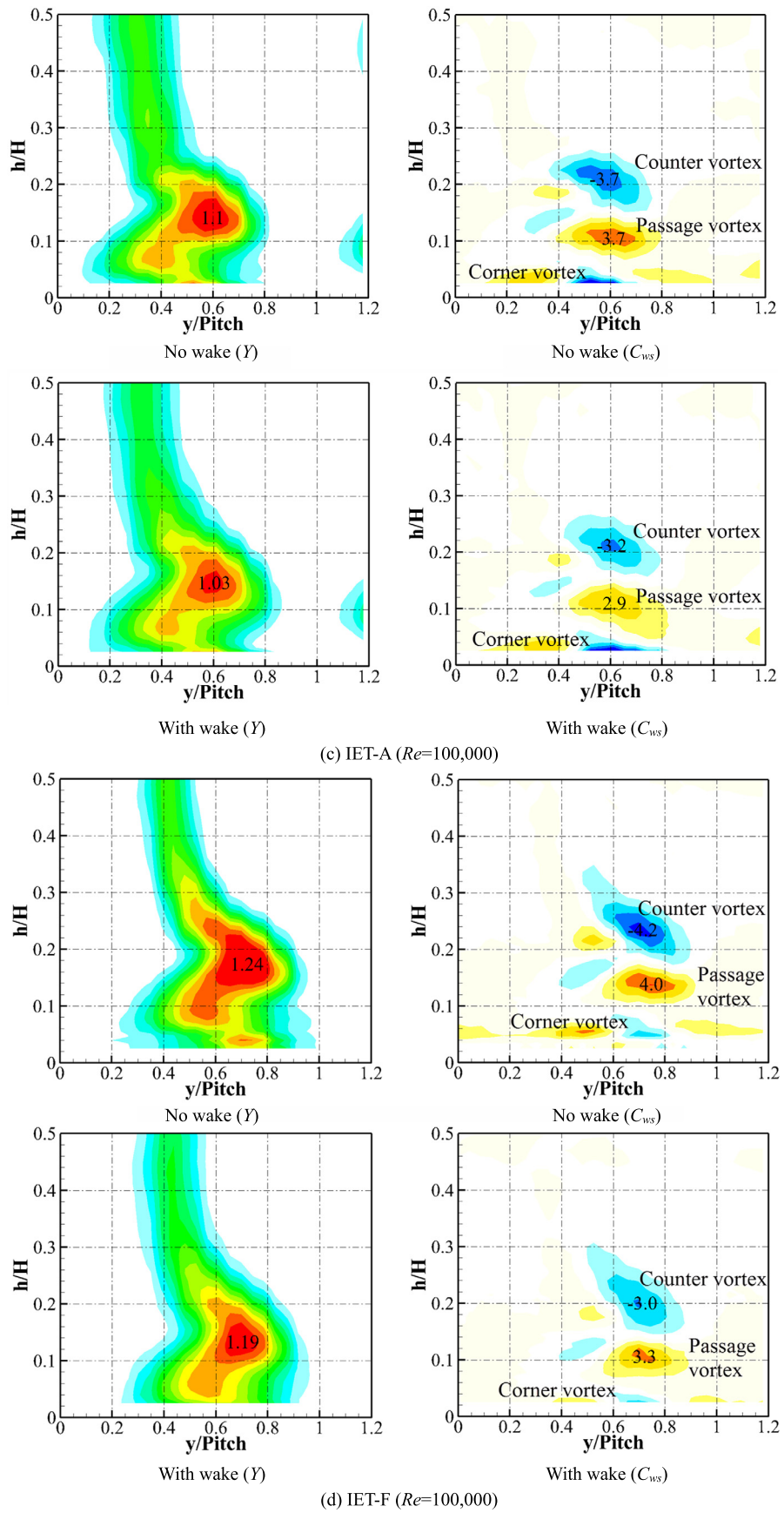
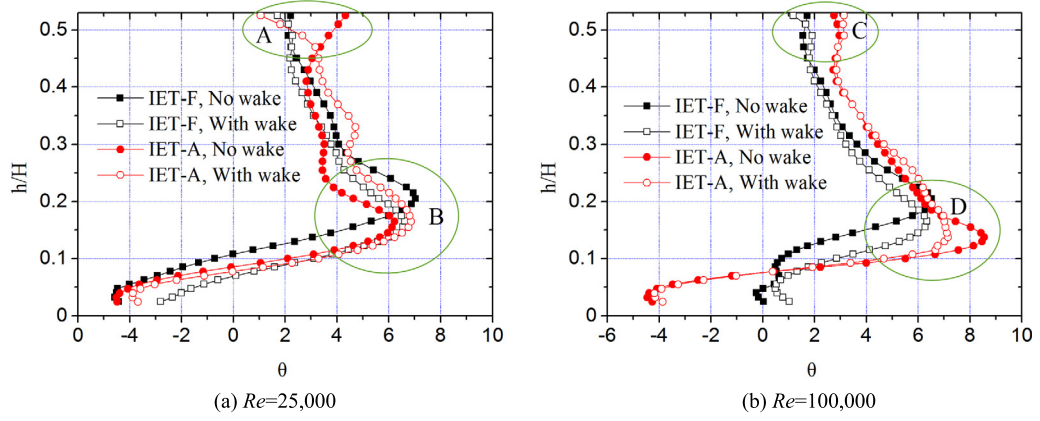


Fig. 12. (continued)



**Fig. 13.** Variation of the pitchwise mass-averaged deviation angle 40% downstream cascade exit.

width of the high-loss region downstream of the cascade was greater and the profile losses were larger for the aft-loaded blade, the secondary losses were smaller, compared to the front-loaded blade. The contour maps of the streamwise vorticity coefficient also demonstrate that the secondary flow was weaker for the aft-loaded blade than for the front-loaded blade. A potential explanation for this is blockage of the flow passage for the aft-loaded blade because of the larger open separation bubble at suction side, leading to lower blade loading as shown in Fig. 8(a); as the cross-passage pressure gradient inside cascade decreased, the secondary flow for the aft-loaded blade was suppressed. The contour maps of the total pressure loss coefficient demonstrated that the upstream wakes increased the peak loss of secondary vortices by 2.8% for the aft-loaded blade and decreased the peak loss of secondary vortices by 8.3% for the front-loaded blade. The incoming wakes increased the strength and size of the counter vortex, and slightly decreased passage vortex strength in the aft-loaded blade passage. In contrast, the upstream wakes decreased the height of secondary flow and the size of the passage vortex and counter vortex in the front-loaded blade passage but slightly increased the passage vortex peak strength, while the corner vortex essentially disappeared. These observations were mainly attributable to suppression of the corner vortex and its movement closer to the endwall under unsteady conditions, and the seven-hole pressure probe can not be applied to obtain the flow field data near endwall. At high  $Re = 100,000$ , the strength of the endwall secondary flow for the aft-loaded blade increased compared to the results at lower Reynolds numbers, which was closely related to blade loading increasing. The suppression of the secondary flow by the incoming wakes was clearly observed. For the aft-loaded blade, the upstream wakes decreased the peaking strength of the passage vortex and counter vortex by 21.6% and 13.5%, respectively. The peak values of the passage vortex and counter vortex for the front-loaded blade decreased by 17.5% and 28.6%, respectively, in the presence of the wakes.

Fig. 13 indicates the variation of the pitchwise mass-averaged outlet deviation angle at 40% of axial chord downstream of the cascade. At the low Reynolds number of 25,000, the outlet deviation angle for the aft-loaded blade increased suddenly near the midspan in the absence of wakes, as indicated by the letter "A" in Fig. 13(a). This phenomenon was mainly ascribed to the open separation bubbles of suction side near the blade midspan, resulting in a larger outlet deviation angle. In contrast, the outlet deviation angle decreased in the vicinity of the endwall owing to weaker secondary flow. Consequently, in the wake region downstream of the cascade appears C-shaped, as observed in the contour map of the total pressure loss coefficient shown in Fig. 12(a). The unsteady wakes significantly suppressed the suction side separation bubble,

greatly decreasing the outlet deviation angle near the midspan, but strengthened the secondary flow, increasing the outlet deviation angle near the endwall. For the front-loaded blade, the incoming wakes reduced the peak value of the outlet deviation angle by suppressing the development of secondary flow, as indicated by the letter "B" in Fig. 13(a). Furthermore, the pitchwise mass-averaged deviation angle distribution was inclined owing to the influence of secondary flow, as also reflected in Fig. 12(b). At the high Reynolds number of 100,000, the outlet deviation angle for the aft-loaded blade near the midspan was clearly higher than that for the front-loaded blade, as indicated by the letter "C" in Fig. 13(b), which resulted from the larger size of the separation bubble for the aft-loaded blade. The unsteady wakes exerted little influence on the outlet deviation angle near the blade midspan. In contrast, near the endwall, the wakes reduced the strength of the secondary flow, resulting in a decreased outlet deviation angle, and the phenomenon of "over turning" was also weaker, as indicated by the letter "D" in Fig. 13(b).

### 3.3. Mechanism analysis via numerical calculations (CFD)

To elucidate the wakes-secondary flow interaction mechanisms in ultra-high-lift LPTs with different blade loading distributions, numerical studies were performed under a Reynolds number of  $Re = 100,000$ . Fig. 14 shows the vortex isosurfaces determined using the  $Q$ -criterion and the variation of the time-averaged total pressure loss coefficient in the cascade passage. The inlet boundary layer was the same for the aft-loaded and front-loaded blades and was obtained from experimental measurements. In the absence of wakes, the pressure side leg of the horseshoe vortex ( $V_{ph}$ ) and suction side leg of the horseshoe vortex ( $V_{sh}$ ) in the front-loaded blade passage were greater than aft-loaded blade passage owing to the higher blade loading for the front-loaded blade. The passage vortex and counter vortex originated from  $V_{ph}$  and  $V_{sh}$ , respectively. Therefore, the secondary flow was stronger in the front-loaded cascade than in the aft-loaded cascade. Furthermore, it can be seen from Fig. 14(a) that the  $V_{ph}$  in the aft-loaded blade passage was very complex compared to that in the front-loaded blade passage, which can mainly be ascribed to the weaker cross-passage pressure gradient at the front portion of the aft-loaded blade, compared to that for the front-loaded blade. This resulted in insufficient driving force for  $V_{ph}$  formation in the aft-loaded blade passage, such that the low-momentum fluid inside the endwall boundary layer could only be rolled up to form a weaker and complex  $V_{ph}$ . Under unsteady conditions, the incoming wakes decreased the strength of  $V_{ph}$  and  $V_{sh}$  and suppressed the passage vortex.

It is generally known that the flow velocity on the blade surface is equal to zero, which means no streamline exists. Limiting

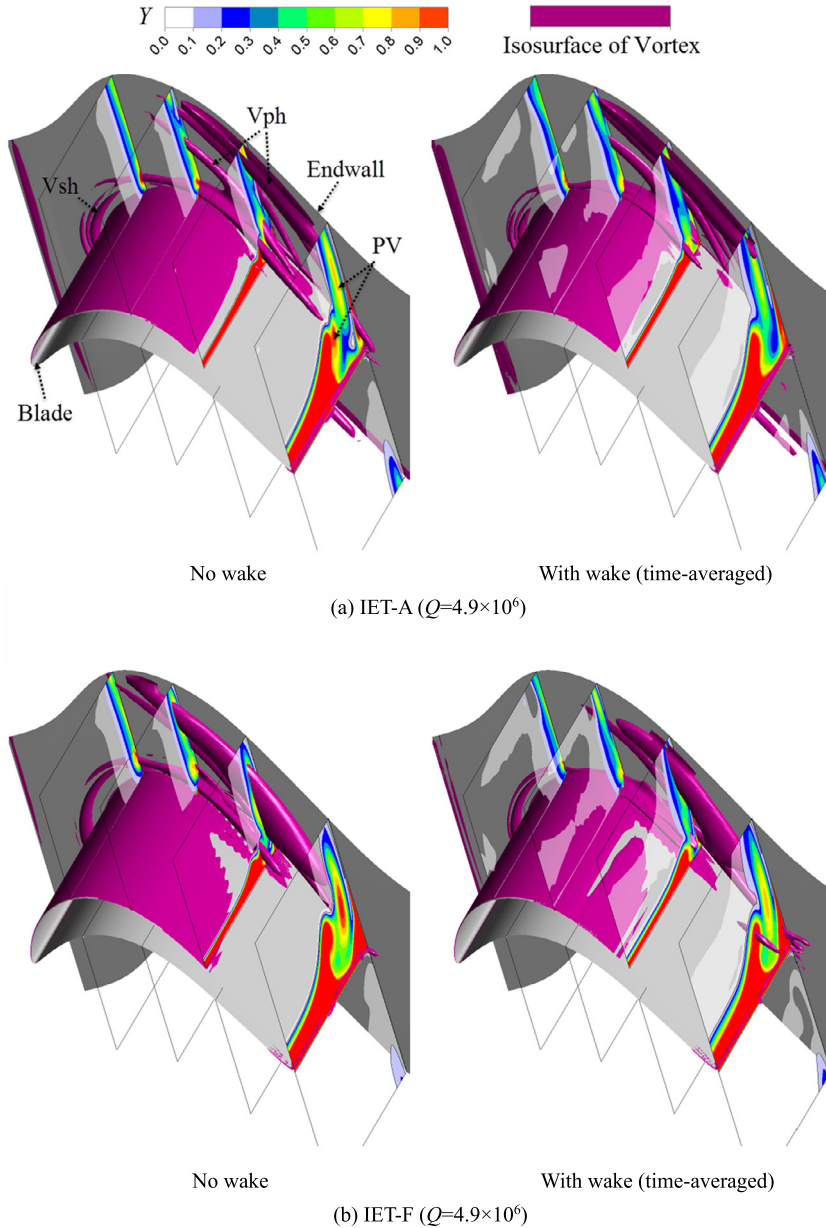


**Fig. 14.** Vortex isosurfaces determined using the  $Q$ -criterion and variation of the time-averaged total pressure loss coefficient in the cascade passage.

streamline is such a kind of streamline, of which the distance to the body surface is close but not equal to zero, so the limiting streamline actually reflects the movement of fluid micelle infinite close to the body surface. Additionally, separation line is determined through the envelope of converging streamlines [35]. The more uniform distribution of limiting streamline usually indicates that flow characteristics are better. Fig. 15 shows time-averaged limiting streamlines on the blade suction surface.  $S$  and  $H$  were lines of separation and reattachment, respectively.  $S_{25}$ ,  $R_2$  and  $S_3$  were migration path of the suction leg of the horseshoe vortex, corner vortex and passage vortex, respectively. It can be seen that the unsteady wakes affected both the suction surface separation bubble and secondary flow, and the secondary vortices and separation bubble interacted with each other. For the aft-loaded blade, a portion of the low-momentum fluid inside  $S_{25}$  was involved in the separation bubble, thereby increasing mixing losses. The gathering phenomenon of the limiting streamlines was more uniform in the presence of wakes, as indicated by the letters "A" and "B" in Fig. 15. Furthermore, the separation bubble reattachment line ( $R_1$ )

moved forward in the presence of incoming wakes. For the front-loaded blade, there were recirculation regions near blade trailing edge at 20% span, as indicated by the letters "C" and "D", which were caused by leakage flow of the pressure surface. The separation bubble essentially disappeared in the presence of unsteady wakes, and the recirculation region was relatively small, which is beneficial for decreasing secondary losses. Furthermore, the unsteady wakes also delayed the originating position of the suction surface separation line for both IET-A and IET-F, as indicated by the letter "M" in Fig. 15, demonstrating the suppressed development of the passage vortex.

After convergence of calculation, the instantaneous results of the last calculated period were output. Fig. 16 shows the instantaneous results of the three-dimensional vortex isosurfaces determined using the  $Q$ -criterion, which are useful for tracing the generation and development process of secondary vortices for different blade loading distributions. The turbulence kinetic energy (TKE) at the blade midspan is shown to help trace the positions of the periodic wakes. Plane 1–6 were uniformly distributed along

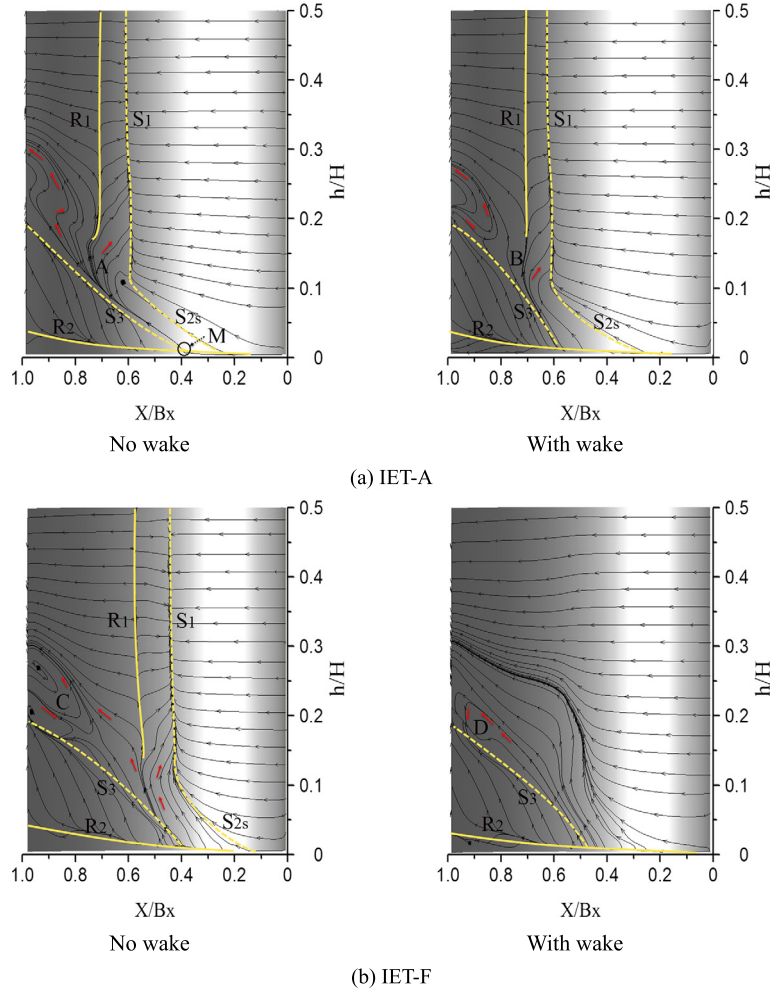


**Fig. 15.** Limiting streamlines on the blade suction surface.

axial chord, which were overlaid contour maps of total pressure loss coefficient ( $Y$ ). At  $t/\tau = 1/3$ , the unsteady wakes were observed to migrate to the blade center and started to interact with  $V_{ph}$ . The incoming wakes caused  $V_{ph}$  to be transported to the suction surface in advance, and  $V_{ph}$  moved near the suction surface earlier for the front-loaded blade passage than for the aft-loaded blade passage. At  $t/\tau = 2/3$ , the upstream wake had moved near to plane 5. The size of  $V_{ph}$  decreased significantly near the position of wake passing. At  $t/\tau = 1$ , the upstream wake had moved the blade trailing edge to interact with the passage vortex, and the passage vortex was clearly suppressed. Meanwhile, the incoming wakes also led to greater mixing losses, as indicated by the letters "A" and "B" in Fig. 16. Furthermore, wake 2 had started to enter the cascade passage, and the strength of  $V_{ph}$  had recovered near plane 4 (between wakes 1 and 2), as indicated by the letters "C" and "D" in Fig. 16. Therefore, it is necessary to optimize the wake passing frequency to continuously suppress the secondary flow, which will be discussed in detail in the subsequent paper of this series.

#### 4. Conclusions

Comprehensive experimental and numerical studies were performed to elucidate the effect of the blade loading distribution on the secondary flow and separation bubbles in ultra-high-lift LPT cascades in both the presence and absence of incoming wakes. The mechanisms responsible for the effect of the blade loading distri-

bution on the secondary flow in the presence of wakes were also examined in detail. The conclusions can be summarized as follows:

(1) At the midspan: At low  $Re = 25,000$ , the suction surface in the ultra-high-lift LPT cascade underwent earlier separation, especially for the aft-loaded blade, for which the separation bubble was no longer attached. Superior two-dimensional aerodynamic performance was observed for the front-loaded blade than for the aft-loaded blade, owing to the shorter diffuser length and weaker adverse pressure gradient. Incoming wakes significantly decreased the size of the separation bubble, leading to a clear improvement in the flow characteristics of the cascade passage and increased blade loading for the aft-loaded blade. At high  $Re = 100,000$ , the profile losses for the aft-loaded and front-loaded blade passages were smaller and similar. Under these conditions, the influence of the unsteady wakes was not readily apparent, and the introduction of low-momentum fluid resulted in decreased blade loading. The mixing loss in the passage increased owing to turbulent viscous dissipation of the wakes, particularly in the case of the front-loaded blade.

(2) At the endwall: At low  $Re = 25,000$ , the secondary flow was weaker for the aft-loaded blade than for the front-loaded blade owing to blockage of the flow passage of the aft-loaded blade due to the larger open separation bubble on the suction surface, and the cross-passage pressure gradient of the cascade decreased. The outlet deviation angle of the aft-loaded blade decreased owing to the interaction between open separation bubbles and secondary flow near the endwall, such that in the high-loss region downstream of the cascade appears C-shaped. At high  $Re = 100,000$ ,

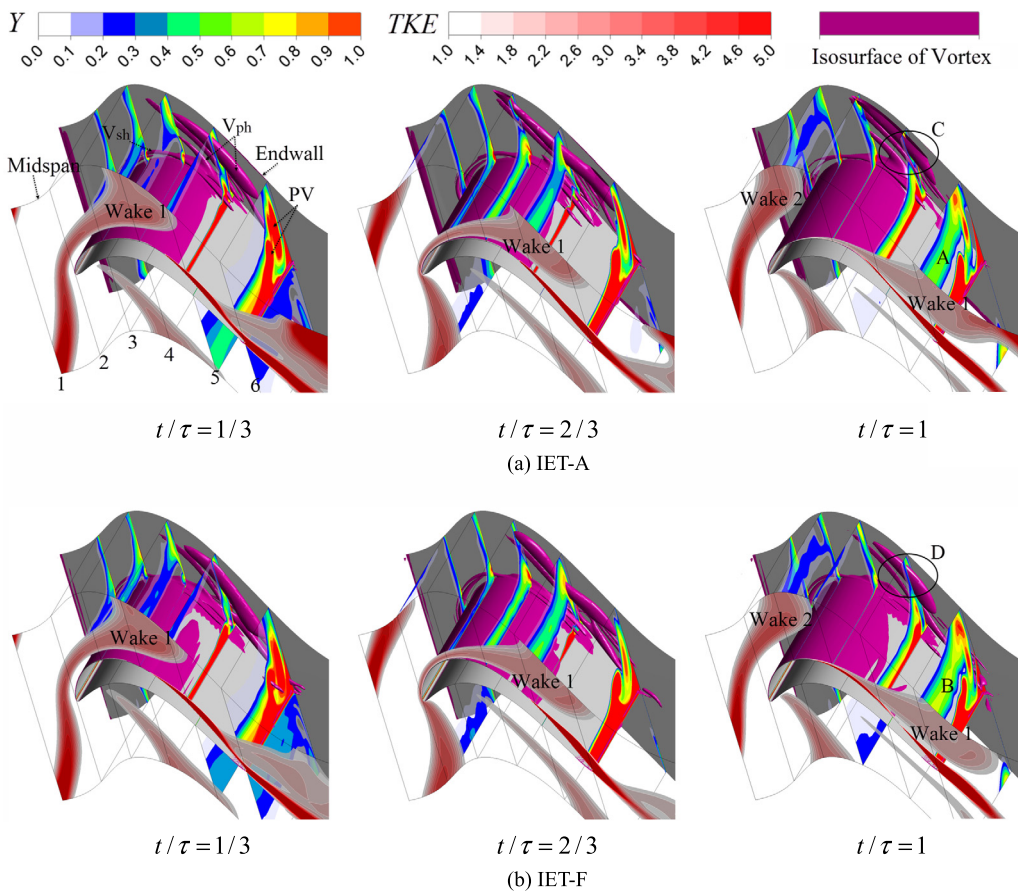


**Fig. 16.** Secondary vortex isosurfaces determined using the  $Q$ -criterion ( $Q = 4.9 \times 10^6 \text{ s}^{-2}$ ), the dimensionless streamwise vorticity ( $C_{ws}$ ) in the cascade passage, and the TKE contours at the midspan.

the strength of the endwall secondary flow for the aft-loaded blade was higher than that at lower Reynolds number, which was closely related to the increased blade loading. The secondary flow was greater in the front-loaded blade passage than in the aft-loaded blade passage, because the position of maximum blade loading was near the front portion of the blade for the front-loaded blade, and the cross-passage pressure gradient rapidly increased, thereby strengthening the pressure side leg of the horseshoe vortex. Upstream wakes also delayed the originating position of passage vortex in both the front-loaded and aft-loaded blade passages, and the secondary flow was clearly suppressed. The experimental results indicated that the incoming wakes decreased the strengths of the passage vortex core and counter vortex core in the aft-loaded blade passage by 21.6% and 13.5%, respectively, and decreased the strengths of the passage vortex and counter vortex in the front-loaded blade passage by 17.5% and 28.6%, respectively.

#### Declaration of competing interest

There is no.

#### Acknowledgement

Financial support for this work was provided by the National Natural Science Foundation of China (Project Nos.: 51876202, 51836008) and is greatly appreciated.

#### References

- [1] C. Bernardini, S.I. Benton, J.-P. Chen, J.P. Bons, Exploitation of subharmonics for separated shear layer control on a high-lift low-pressure turbine using acoustic forcing, *J. Turbomach.* 136 (2014) 051018.
- [2] E. Göttlich, Research on the aerodynamics of intermediate turbine diffusers, *Prog. Aerosp. Sci.* 47 (2011) 249–279.
- [3] E. Curtis, H. Hodson, M. Banieghbal, J. Denton, R. Howell, N. Harvey, Development of blade profiles for low-pressure turbine applications, *J. Turbomach.* 119 (1997) 531–538.
- [4] R.J. Howell, H.P. Hodson, V. Schulte, R.D. Stieger, H.P. Schiffer, F. Haselbach, N.W. Harvey, Boundary layer development in the BR710 and BR715 LP turbines: the implementation of high lift and ultra high lift concepts, *J. Turbomach.* 124 (2002) 385–392.
- [5] J. Gier, M. Franke, N. Hubner, T. Schroder, Designing low pressure turbines for optimized airfoil lift, *J. Turbomach.* 132 (2010) 12.
- [6] R.E. Mayle, The 1991 IGTI scholar lecture: the role of laminar-turbulent transition in gas turbine engines, *J. Turbomach.* 113 (1991) 509–536.
- [7] S. Sun, Z.J. Lei, X.G. Lu, S.F. Zhao, J.Q. Zhu, An experimental study of separation control on ultra-highly-loaded low pressure turbine blade by surface roughness, *J. Therm. Sci.* 24 (2015) 229–238.
- [8] R.J. Volino, Separation control on low-pressure turbine airfoils using synthetic vortex generator jets, *J. Turbomach.* 125 (2003) 765–777.
- [9] J.H. Huang, T.C. Corke, F.O. Thomas, Plasma actuators for separation control of low-pressure turbine blades, *AIAA J.* 44 (2006) 51–57.
- [10] P.W. Bearman, J.K. Harvey, Control of circular cylinder flow by the use of dimples, *AIAA J.* 31 (1993) 1753–1756.
- [11] E. Sobhani, M. Ghaffari, M.J. Maghrebi, Numerical investigation of dimple effects on Darrieus vertical axis wind turbine, *Energy* 133 (2017) 231–241.
- [12] K.N. Kumar, M. Govardhan, Numerical study of effect of streamwise end wall fences on secondary flow losses in two dimensional turbine rotor cascade, *Eng. Appl. Comput. Fluid Mech.* 4 (2010) 580–592.
- [13] H. Sauer, R. Müller, K. Vogeler, Reduction of secondary flow losses in turbine cascades by leading edge modifications at the endwall, *J. Turbomach.* 123 (2000) 207–213.
- [14] G.A. Zess, K.A. Thole, Computational design and experimental evaluation of using a leading edge fillet on a gas turbine vane, *J. Turbomach.* 124 (2002) 167–175.
- [15] K. Ananthakrishnan, M. Govardhan, Influence of fillet shapes on secondary flow field in a transonic axial flow turbine stage, *Aerospace Sci. Technol.* 82 (2018) 425–437.

- [16] K. Sangston, J. Little, M.E. Lyall, R. Sondergaard, End wall loss reduction of high lift low pressure turbine airfoils using profile contouring-part II: validation, *J. Turbomach.* 136 (2014) 10.
- [17] C. Zhang, K.S. Bijay, Investigation on drag reduction performance of aero engine blade with micro-texture, *Aerosp. Sci. Technol.* 72 (2018) 380–396.
- [18] A.P. Weiss, L. Fottner, The influence of load distribution on secondary flow in straight turbine cascades, *J. Turbomach.* 117 (1995) 133–141.
- [19] T. Zoric, I. Popovic, S.A. Sjolander, T. Praisner, E. Grover, Comparative investigation of three highly loaded LP turbine airfoils: part I – measured profile and secondary losses at design incidence, in: ASME Turbo Expo 2007: Power for Land, Sea, and Air, Montreal, Canada, May 2007, paper no. GT2007-27538.
- [20] M.W. McQuilling, Design and Validation of a High-Lift Low-Pressure Turbine Blade, Ph.D. Dissertation, Wright State Univ., Dayton, OH, 2007.
- [21] V. Schulte, H.P. Hodson, Unsteady wake-induced boundary layer transition in high lift LP turbines, *J. Turbomach.* 120 (1998) 28–35.
- [22] Y. Liang, Z.P. Zou, H.X. Liu, W.H. Zhang, Experimental investigation on the effects of wake passing frequency on boundary layer transition in high-lift low-pressure turbines, *Exp. Fluids* 56 (2015) 13.
- [23] V. Michelassi, L.W. Chen, R. Pichler, R.D. Sandberg, Compressible direct numerical simulation of low-pressure turbines-part II: effect of inflow disturbances, *J. Turbomach.* 137 (2015) 12.
- [24] L. Davide, D. Simoni, M. Ubaldi, P. Zunino, F. Bertini, Coherent structures formation during wake-boundary layer interaction on a LP turbine blade, *Flow Turbul. Combust.* 98 (2017) 57–81.
- [25] C.M. Schneider, D. Schrack, M. Kuerner, M.G. Rose, S. Staudacher, Y. Guendogdu, U. Freygang, On the unsteady formation of secondary flow inside a rotating turbine blade passage, *J. Turbomach.* 136 (2014) 10.
- [26] R. Ciocciari, I. Kirik, R. Niehuis, Effects of unsteady wakes on the secondary flows in the linear T106 turbine cascade, *J. Turbomach.* 136 (2014) 11.
- [27] X. Qu, Y.F. Zhang, X.G. Lu, G. Han, Z.L. Li, J.Q. Zhu, Effects of periodic wakes on the endwall secondary flow in high-lift low-pressure turbine cascades at low Reynolds numbers, *Proc. Inst. Mech. Eng., G J. Aerosp. Eng.* 233 (2019) 354–368.
- [28] L. Qi, Z.P. Zou, H.X. Liu, W. Li, Upstream wake-secondary flow interactions in the endwall region of high-loaded turbines, *Comput. Fluids* 39 (2010) 1575–1584.
- [29] L.M. da Silva, J.T. Tomita, C. Bringhenti, Numerical investigation of a HPT with different rotor tip configurations in terms of pressure ratio and efficiency, *Aerosp. Sci. Technol.* 63 (2017) 33–40.
- [30] Ö.H. Turgut, C. Camci, A nonaxisymmetric endwall design approach and its computational assessment in the NGV of an HP turbine stage, *Aerosp. Sci. Technol.* 47 (2015) 456–466.
- [31] K. Kiran, S. Anish, An investigation on the effect of pitchwise endwall design in a turbine cascade at different incidence angles, *Aerosp. Sci. Technol.* 71 (2017) 382–391.
- [32] D.G. Gregorysmith, C.P. Graves, J.A. Walsh, Growth of secondary losses and vorticity in an axial turbine cascade, *J. Turbomach.* 110 (1988) 1–8.
- [33] X. Lu, Y. Zhang, W. Li, S. Hu, J. Zhu, Effects of periodic wakes on boundary layer development on an ultra-high-lift low pressure turbine airfoil, in: Proceedings of the Institution of Mechanical Engineers, Part A, *J. Power Energy* 231 (2017) 25–38.
- [34] F. Montomoli, H. Hodson, F. Haselbach, Effect of roughness and unsteadiness on the performance of a new low pressure turbine blade at low Reynolds numbers, *J. Turbomach.* 132 (2010) 031018.
- [35] C.T. Tai, Determination of three-dimensional flow separation by a streamline method, *AIAA J.* 19 (1981) 1264–1271.